MATERIALS SCIENCE

Direct coherent multi-ink printing of fabric supercapacitors

Jingxin Zhao[1]*, Hongyu Lu[2]*, Yan Zhang[3]*, Shixiong Yu[4]*, Oleksandr I. Malyi[5], Xiaoxin Zhao[4], Litong Wang[1], Huibo Wang[1], Jianhong Peng[2†], Xifei Li[2], Yanyan Zhang[1,6], Shi Chen[1], Hui Pan[1], Guichuan Xing[1], Conghua Lu[7], Yuxin Tang[1,6†], Xiaodong Chen[8†]

Coaxial fiber-shaped supercapacitors with short charge carrier diffusion paths are highly desirable as high-performance energy storage devices for wearable electronics. However, the traditional approaches based on the multistep fabrication processes for constructing the fiber-shaped energy device still encounter persistent restrictions in fabrication procedure, scalability, and mechanical durability. To overcome this critical challenge, an all-in-one coaxial fiber-shaped asymmetric supercapacitor (FASC) device is realized by a direct coherent multi-ink writing three-dimensional printing technology via designing the internal structure of the coaxial needles and regulating the rheological property and the feed rates of the multi-ink. Benefitting from the compact coaxial structure, the FASC device delivers a superior areal energy/power density at a high mass loading, and outstanding mechanical stability. As a conceptual exhibition for system integration, the FASC device is integrated with mechanical units and pressure sensor to realize high-performance self-powered mechanical devices and monitoring systems, respectively.

INTRODUCTION

The development of advanced fibrous energy storage devices with excellent knittability, splendid flexibility, and high mechanical stability is highly demanded to advance textile-based wearable electronics (*1*, *2*). As one of the most promising fiber-shaped energy storage devices, fiber-shaped asymmetric supercapacitors (FASCs) have been widely applied in wearable electronics, which is attributed to their high-power density, long cycling stability, excellent reversibility, and improved energy density (*3*–*7*). Currently, the parallel, twisted, and coaxial architectures of FASCs have been explored to improve the supercapacitor performance (*8*–*18*). Compared to coaxial architectures, the parallel and twisted architectures are not ideal structures for the electron transfer and ion diffusion within the electrode materials because of their larger spacing between the two electrodes. In addition, the parallel-shape FASCs have a massive volume structure, posing a serious challenge for the large-scale integration process (Fig. 1A). While for twisted-shape FASCs, the negative/positive electrodes are more vulnerable to separate when the device is bent and degrade the electrochemical performance because of the increase in charge carrier diffusion paths (Fig. 1B). Although the coaxial FASC (Fig. 1, C and D) with shorter charge carrier paths can improve device performance, they still suffer from the same problem of the twisted device that the two electrodes are easier to separate and then to peel away from the electrode during long-time bending. This is mainly due to loose interface contact between each layer (positive electrode/electrolyte/negative electrode) in coaxial FASC devices during the multistep coating process, and the mismatch of Young's modulus from the loose electrode contact layers is prone to crack during long-time or extremely mechanical bending (*19*, *20*). Furthermore, the fabrication procedure of these coaxial FASC devices undergoes multiple steps with the key concerns on fabrication efficiency, preparation cost, and scalability (*8*, *12*, *13*), which have inhibited their scalable production and further application in energy storage fields. To overcome the above challenges, the development of a direct and scalable approach to construct compact coaxial FASC devices with short charge carrier diffusion length and intimate interface contact alleviating the mismatch of Young's modulus from electrode layers is highly demanded to achieve high-performance and mechanically robust FASC devices.

As known, high-throughput three-dimensional (3D) printing direct ink writing technology has already been successfully used to construct complex structures because of its advantages such as continuous manufacturing capability, scalability, and low cost, which has been widely applied in various fields, such as biotechnology (*21*, *22*), engineered composites (*23*–*25*), electronic devices (*26*–*28*), and energy storage devices (*29*–*35*). In this light, we foresee that the high-throughput direct 3D printing technology is a promising approach to construct the all-in-one coaxial FASC device with compact internal structures. Although the 3D printing direct ink writing technology has been applied to print asymmetric supercapacitors recently, the full device was obtained by layer-by-layer printing and/or coating process by using different electrode inks/electrolytes, since the traditional direct ink writing technology is based on single-ink printing, which can only write one electrode at one time (*14*). Therefore, an ideal 3D printing ink writing technology enabling viscoelastic multi-ink extruding from one single nozzle to directly build all-in-one coaxial FASC devices is highly desired for building a compact and seamless coaxial FASC device.

[1]Joint Key Laboratory of the Ministry of Education, Institute of Applied Physics and Materials Engineering, University of Macau, Avenida da Universidade, Taipa, Macau SAR 999078, P. R. China. [2]Institute of Advanced Electrochemical Energy, Xi'an University of Technology, Xi'an 710048, P. R. China. [3]Centre of Nanoscale Science and Technology, Key Laboratory of Functional Polymer Materials, Institute of Polymer Chemistry, College of Chemistry, Nankai University, Tianjin 300071, P. R. China. [4]School of Materials Science and Engineering, Tianjin University, Tianjin 300072, P. R. China. [5]Renewable and Sustainable Energy Institute, University of Colorado, Boulder, CO 80309, USA. [6]College of Chemical Engineering, Fuzhou University, Fuzhou 350116, P. R. China. [7]School of Materials Science and Engineering, Tianjin Chengjian University, Tianjin 300384, P. R. China. [8]Innovative Centre for Flexible Devices (iFLEX), School of Materials Science and Engineering, Nanyang Technological University, 50 Nanyang Avenue, Singapore 639798, Singapore.
*These authors contributed equally to this work.
†Corresponding author. Email: chenxd@ntu.edu.sg (X.C.); yxtang@fzu.edu.cn (Y.T.); pjhhj@sohu.com (J.P.)

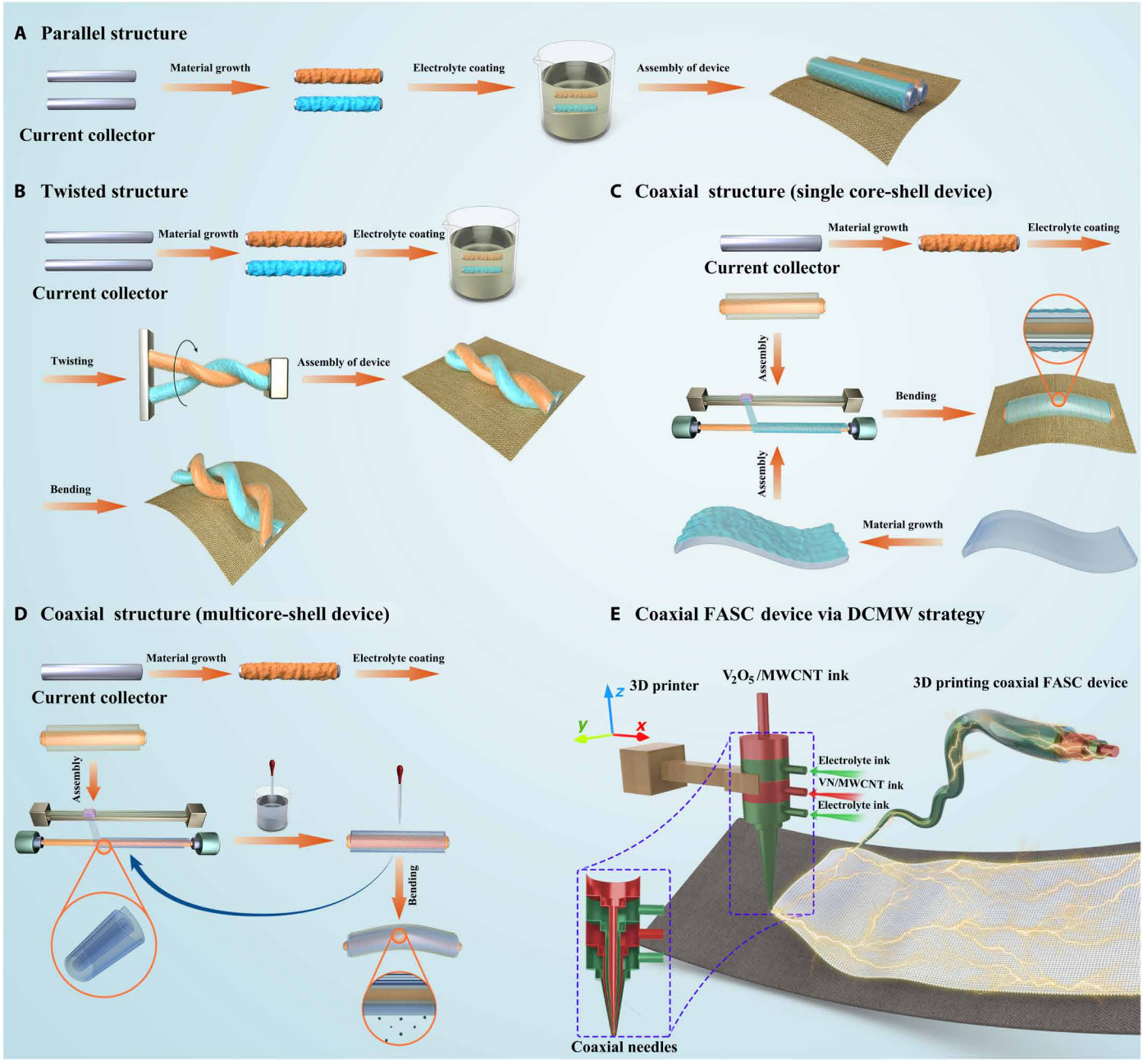

Fig. 1. Diagrammatic drawing of the fabrication process of various FASC devices. Schematic diagram of the comparison of the preparation process of the conventional FASC device with (**A**) parallel, (**B**) twisted, (**C and D**) coaxial architectures, and (**E**) our development of three-dimensional (3D) printing coaxial FASC device via a direct coherent multi-ink writing (DCMW) technology.

As a conceptual exhibition, an all-in-one 3D printing coaxial FASC device was rationally designed via 3D printing direct coherent multi-ink writing (DCMW) (Fig. 1E) via designing the structure of the coaxial needles and regulating the rheological property and the feed rates of the multi-ink. That is, the internal structure of the multicore-shell needles is designed by following the principle of the charge match of the different electrodes, and the rheological properties of the multi-inks should match each other with the gradual increase of feed rates from the innermost layer to the outermost layer during 3D printing. The compact four-layer structure of the as-prepared device shortens the ion diffusion path, improving the electrochemical performance and mechanical durability of the device under bending. In our proof-of-concept FASC device, the V_2O_5 nanowires (NWs)/multiwalled carbon nanotubes (MWCNTs) and vanadium nitride (VN) NWs/MWCNTs are served as positive and negative electrodes, respectively. The as-printed FASC device embraces a large operating voltage of 1.6 V, a high areal specific capacitance (C_A) of 152.7 mF cm^{-2} [with a volumetric specific capacitance (C_V) of 27.8 F cm^{-3} and a gravimetric specific capacitance (C_g) of 59.3 F g^{-1}], and an ultrahigh areal energy density (E_A) of 54.3 μWh cm^{-2} [with a volumetric energy

density (E_V) of 9.9 F cm^{-3} and a gravimetric energy density (E_g) of 21.1 Wh kg^{-1}] at a high mass loading of 16.4 mg cm^{-2}. This performance is surpassing most of the currently reported 3D printing supercapacitor devices (table S1, Supplementary Materials). Impressively, the device exhibits splendid flexibility and excellent mechanical performance with capacitance retention of 95.5% after 5000 cycles of repetitive bending, which is better than traditional coaxial (87.1%) or twisted (78.2%) architecture asymmetric supercapacitors. In addition, our 3D printing coaxial FASC device can provide the power to realize the self-powered mechanical device and monitoring system, exhibiting stable power output and press sensing performance, respectively. This strategy offers a universal strategy to design on-demand fibrous energy storage devices for high-performance wearable electronics.

RESULTS

Fabrication process of an all-in-one 3D printing coaxial FASC device and the rheological properties of the inks

First, the positive (V_2O_5 NWs) and negative electrodes (VN NWs) were synthesized for building the high–energy density FASC device because of their high theoretical capacities and broad operating potential windows (*14*). To uncover the microstructure and morphology of the samples, we used field-emission scanning electron microscopy (FESEM) and transmission electron microscopy (TEM). Figure S1A [scanning electron microscopy (SEM) image], fig. S1B (TEM image), and fig. S1D [x-ray diffraction (XRD)] clearly depict the formation of the V_2O_5 NWs (diameter, ≈200 nm; length surpass, 10 μm) (Supplementary Materials). A lattice distance of 0.34 nm is obtained in the high-resolution TEM image (fig. S1C, Supplementary Materials), which belongs to the (110) crystallographic plane of the V_2O_5. Energy-dispersive spectroscopy mapping (fig. S1E, Supplementary Materials) further confirms the formation of the V_2O_5. To survey the surface element of the prepared samples, we applied x-ray photoelectron spectroscopy (XPS). Figure S1F reveals the formation of the V_2O_5 product. Three characteristic peaks at 517.5, 524.8, and 530.3 eV are shown in fig. S2 (A and B) (Supplementary Materials), which belong to the binding energy of V $2p^3$, V $2p^1$, and O 1s electrons, respectively (*10*, *36*, *37*). In addition, the structural characterizations (SEM and TEM) of the sample confirm the formation of the VN, which are shown in fig. S3 (A to D) (see details in section S1.2, Supplementary Materials).

The preparation diagrammatic drawing of the 3D printing coaxial FASC device is depicted in Fig. 1E. The video of the fabrication process for printing the device is provided in movie S1 (Supplementary Materials). The desired 3D printing coaxial FASC devices are rationally designed on the basis of the following considerations. First, the multicore-shell printheads were designed and fabricated for constructing the 3D printing device, and the feed rate (see details in section S1, Supplementary Materials) is gradually increased from the innermost layer to the outermost layer for maintaining the same printing rate. Second, printed electrode material "inks" were fabricated by regulating the proportion of the active substances (V_2O_5 or VN NWs) and MWCNTs to obtain the homogeneous, highly viscous, and optimized elastic ink. Meanwhile, the viscousness of the gel electrolyte inks should be less than that of the electrode material inks. Moreover, the viscosity roughly matches so that the printing rate does not interfere with each other. Third, the quick solidification process is necessary to form the 3D printing coaxial FASC device. Last, the inner structure (surface area and diameter) of the printed device was confirmed by following the principle of charge match of the negative and positive electrodes. On the basis of these considerations, the as-fabricated coherent multi-inks [V_2O_5 NWs/MWCNTs, VN NWs/MWCNTs, and polyvinyl alcohol (PVA)/KOH] with good rheological behavior served as the 3D printable inks as demanded (Fig. 2A). After 3D printing, the as-fabricated coaxial FASC device can be achieved via the fast solidification of polyvinylidene fluoride (PVDF)/*N*-methyl-2-pyrrolidone (NMP), and then NMP solvents were removed by washing with ethanol and water and dried at room temperature (Fig. 2B). The introduction of PVDF is mainly to increase the viscosity of the NMP solvent and reduce the slip of the coaxial device in the solidification bath, thus better maintaining device morphology. To obtain the printable MWCNT-based and electrolyte inks for achieving an all-in-one 3D printing coaxial FASC device, the composition and rheology behavior (such as highly viscous, non-Newtonian fluids) of the inks need to be tuned so that the inks can be successfully extruded, and the self-supporting pattern is well maintained. Figure 2C exhibits the apparent viscosity of the dispersed MWCNT suspensions as a function of shear rate, indicating that the MWCNT suspension at 200 mg ml^{-1} is non-Newtonian fluid with shear-thinning behavior, which is suitable to the extrusion processing of the printable ink (*16*). Compared with the pristine MWCNTs, the MWCNT-based hybrid inks (V_2O_5 NWs/MWCNTs or VN NWs/MWCNTs) embrace the slightly higher apparent viscosity with strong shear-thinning behavior when the V_2O_5 or VN NWs were added, which results from the orientation of the MWCNTs and electrochemical active substances (V_2O_5 or VN) during the 3D printing extrusion process (Fig. 2, D and E). Obviously, all the ink behaviors are well explained by the Herschel-Bulkley model (*38*)

$$\tau = \eta(\xi)\,\xi = \lambda + K\,\xi^{n} \quad (1)$$

where τ, η, ξ, and λ represent shear thinning, apparent viscosity, shear rate, and shear stress, respectively. Accordingly, all the inks conform to the shear-thinning behavior, and the values of the viscosity are suitable for printing. Figure 2 (F to H) displays the dynamic mechanical analysis (DMA) of the as-prepared inks with oscillation range from 0.1 to 10^3 Pa at 1.0 Hz. The storage and loss moduli of the inks demonstrate the stored energy from the elastic contribution and the dissipated energy from the viscous contribution, respectively. The symbols of the storage and loss moduli are filling shapes and open shapes, respectively. The point of intersection of the storage and loss moduli is called the yield point. The storage moduli of all the inks (MWCNTs, V_2O_5 NWs/MWCNTs, and VN NWs/MWCNTs) are greater than their loss moduli under the value of the yield point, reflecting a solid-like behavior. On the basis of the solid-like property, the ink materials can maintain shape when it leaves the nozzle after being extruded, making it possible to achieve the coaxial structure of the fiber device. The loss moduli of all the inks decrease lower than the elastic moduli, indicating a fluid-like behavior. Within this region, the inks mainly show viscous deformation, which is attributed to the extrusion process of 3D printing. Moreover, the good rheological property of the electrolyte ink is also obtained (fig. S4, Supplementary Materials). On the basis of the excellent rheological behavior (such as highly viscous, non-Newtonian fluids) of the MWCNT-based and electrolyte inks, an all-in-one 3D printing coaxial FASC device is expected to be successfully fabricated.

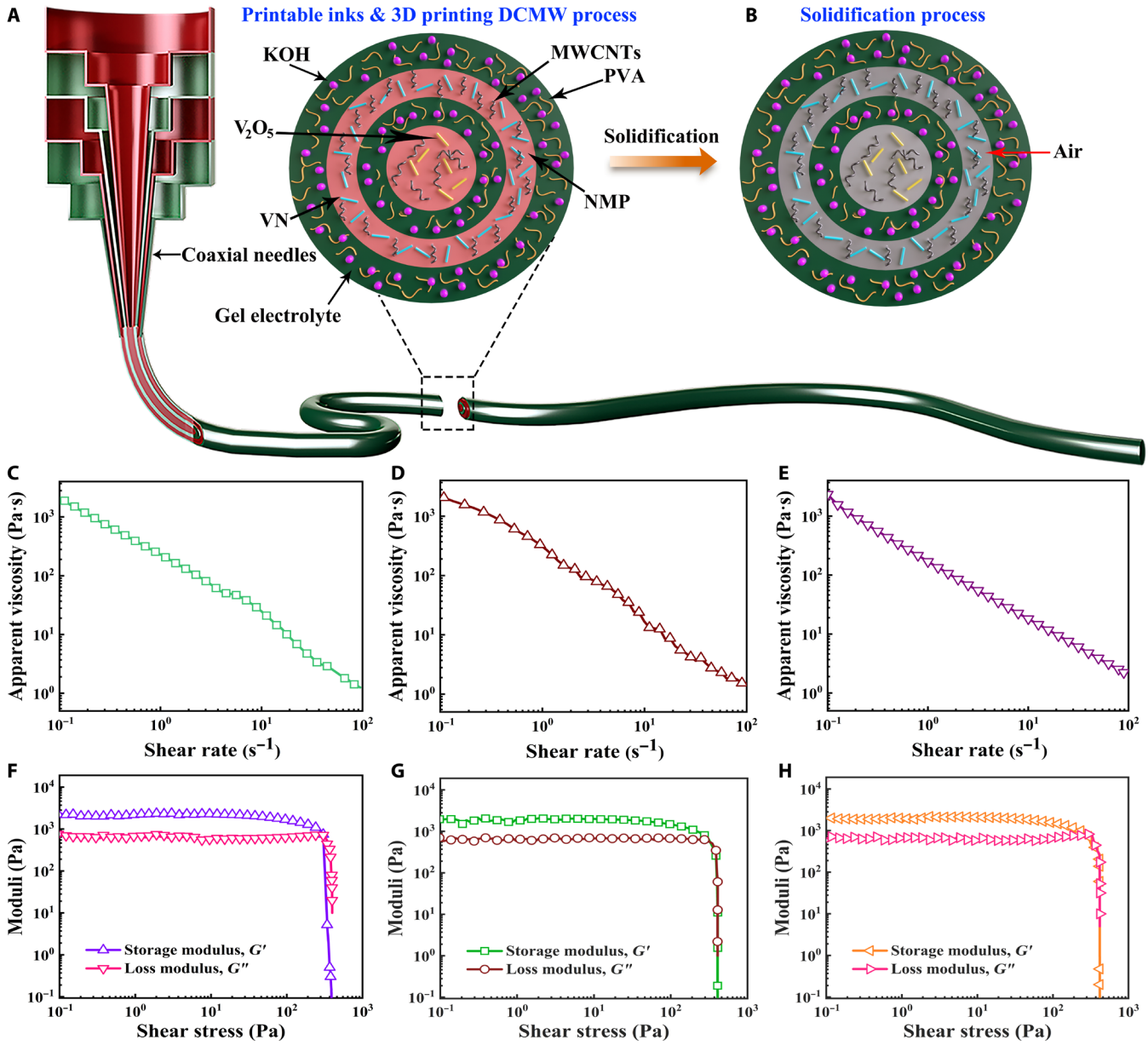

Fig. 2. Rheological performance of the as-fabricated inks. (**A**) 3D printing extrusion process of the printable coaxial FASC device. (**B**) 3D printing coaxial FASC device is achieved by subsequent solidification process. Rheological properties of pure MWCNT, V_2O_5 NW/MWCNT, and VN NW/MWCNT slurry inks. (**C to E**) Apparent viscosity as a function of shear rate for pure MWCNT, V_2O_5 NW/MWCNT, and VN NWs/MWCNT inks, respectively. (**F to H**) Storage modulus, *G*′, and loss modulus, *G*″, as a function of shear stress for pure MWCNT, V_2O_5 NW/MWCNT, and VN NW/MWCNT slurry inks, respectively.

Characterization of the 3D printing coaxial FASC device

For probing the structure of the as-prepared device, schematic illustrations of the cross-sectional view and cross-sectional SEM images of the V_2O_5 NW/MWCNT fiber, V_2O_5 NW/MWCNTs@gel electrolyte fiber, V_2O_5 NW/MWCNTs@gel electrolyte@VN NW/MWCNT fiber, and the coaxial FASC device by 3D printing DCMW technology are demonstrated in Fig. 3 (A to H). The cross-sectional SEM images in Fig. 3E and fig. S5B exhibit the single V_2O_5 NW/MWCNT fiber with a diameter of 250 μm, and the single fiber embraces a relatively compact structure without the big pores (Supplementary Materials). The SEM images of the pure MWCNTs and VN NW/MWCNT fibers are shown in fig. S5 (A and C) (Supplementary Materials). The phase composition and chemical states of the VN NW/MWCNT ink are confirmed by XRD and XPS (figs. S6 and S7, Supplementary Materials), and the Raman spectra of the V_2O_5 NW/MWCNT and VN NW/MWCNT inks are depicted in fig. S8 (A and B, respectively), which reveal the characteristic peaks of VO_x and VO_x deposited on VN, and the typical peak of crystalline carbon (Supplementary Materials) (*39*, *40*). It is revealed that the V_2O_5 NW/MWCNT fiber is uniformly encapsulated by the gel electrolyte (Fig. 3F) with the porous structure (fig. S9, Supplementary Materials). This can lead to the single fiber making close contact with the gel electrolyte and

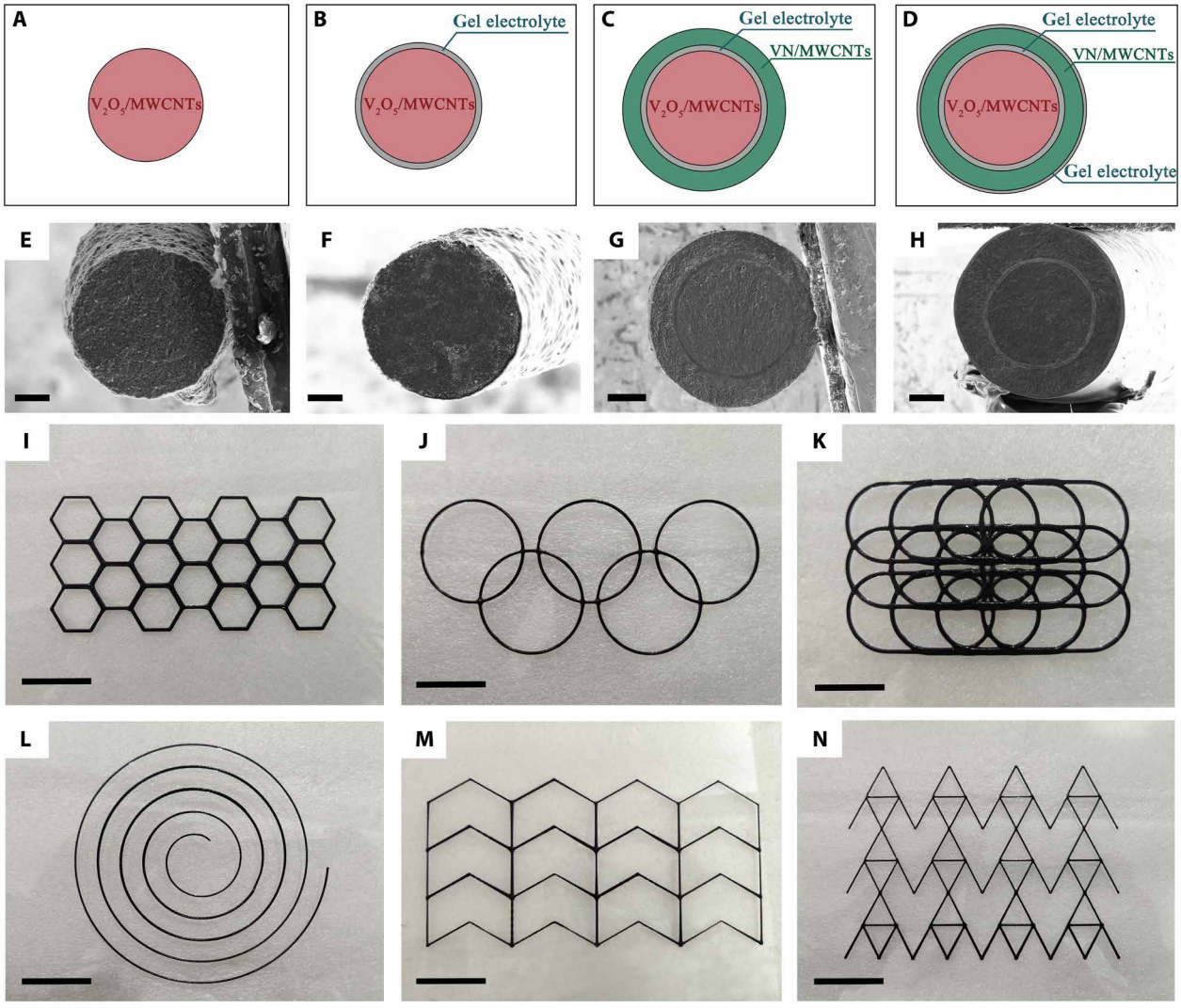

Fig. 3. Structures of the electrode and 3D printing coaxial FASC device. (**A** to **D**) Schematic illustrations of the cross-sectional view of the V_2O_5 NW/MWCNT fiber, V_2O_5 NWs/MWCNTs@gel electrolyte fiber, V_2O_5 NWs/MWCNTs@gel electrolyte@VN NW/MWCNT fiber, and the 3D printing coaxial FASC device struts. The cross-sectional SEM images of (**E**) V_2O_5 NW/MWCNT fiber, (**F**) V_2O_5 NWs/MWCNTs@gel electrolyte fiber, (**G**) V_2O_5 NWs/MWCNTs@gel electrolyte@VN NW/MWCNT fiber, and (**H**) the 3D printing coaxial FASC device by DCMW. (**I** to **N**) The printed FASC device with different patterns. Scale bars, 50 μm (E and F), 100 μm (G and H), and 10 mm (I to N). Photo credit: (I to N) Hongyu Lu, Xi'an University of Technology.

the ease of electrolyte penetration. Figure 3G exhibits the cross-sectional SEM image of the VN NW/MWCNTs@PVA/KOH gel electrolyte@V_2O_5 NW/MWCNT fiber; the diameter of the fiber is about 390 μm. The cross-sectional SEM image of the 3D printing coaxial FASC device is shown in Fig. 3H, the diameter of the as-printed device is about 400 μm, and the printed outer gel electrolyte can effectively prevent the peeling off of the electrode materials. In addition, various complicated patterns (Fig. 3, I to N) were printed by 3D printing DCMW technology, which demonstrates its competence to fabricate 3D printing coaxial FASC device with high accuracy and scalability, and the stress-strain performance results show the excellent flexibility and mechanical strength of the printed fiber electrodes and devices (fig. S10, Supplementary Materials). Moreover, the high Brunauer-Emmett-Teller (BET) surface area of the as-prepared V_2O_5 NW/MWCNT fiber and VN NW/MWCNT fiber can obtain high values of 114.8 and 121.2 $m^2 g^{-1}$, respectively (fig. S11, A and B, Supplementary Materials). The mesopore structures of the V_2O_5 NW/MWCNT fiber and VN NW/MWCNT fiber were obtained on the basis of the pore size distribution (fig. S11, C and D, Supplementary Materials), which is a benefit for the transport and diffusion of electrolyte ions during the fast charge/discharge process.

Electrochemical and flexible performance of the 3D printing coaxial FASC device

To realize a high–energy density 3D printing coaxial FASC device for a flexible wearable device, we selected the proper electrochemical performances of the positive (V_2O_5 NWs/MWCNTs) and the negative (VN NWs/MWCNTs) electrodes by the principle of the charge match. It is worth noting that the as-printed coaxial FASC device embraces outstanding electrochemical performance by designing and adjusting the diameter of the positive and negative aspects of the coaxial needles. The electrochemical performances of the positive

and negative electrodes are exhibited in figs. S12 and S13, respectively (Supplementary Materials). To confirm the working voltage of the fabricated device, the cyclic voltammetry (CV) curves of the negative/positive electrode were tested. The specific operating voltage windows of the positive and negative electrodes are −1.2 to −0.2 V and 0 to 0.4 V (fig. S14, Supplementary Materials), respectively. Thus, the 3D printing coaxial FASC device owns a high working voltage of 1.6 V. The cross-sectional schematic diagram of the 3D printing coaxial FASC device is exhibited in Fig. 4A. Figure 4B shows that the loop region of the CV curves of the 3D printing coaxial FASC device enlarges with the increase in operating voltage range (1.0 to 1.6 V) at a scan rate of 75 mV s^{-1}. The obtained CV curves (Fig. 4B) embrace a quasi-rectangular shape without obvious redox peaks, which indicates excellent capacitive behavior (*12*, *13*, *41*–*44*). To further assess the electrochemical properties of the fabricated 3D printing coaxial FASC device, we also performed galvanostatic charge/discharge (GCD), CV, and electrochemical impedance spectroscopy (EIS) analysis. The CV curves of the as-prepared electrochemical device are demonstrated in Fig. 4C, which retains the quasi-rectangular shape with the scan rate increasing from 5 to 100 mV s^{-1} with an operating voltage window from 0 to 1.6 V, thus indicating an ideal electrocapacitive reversible behavior (*45*, *46*). Impressively, the almost symmetric triangular shapes and excellent rate capability are obtained for the as-prepared FASC device (Fig. 4D), revealing the desired capacitive behavior (*47*–*49*). Correspondingly, the EIS fitting result (fig. S15, Supplementary Materials) also indicates the fast charge carrier diffusion in the device, since the diffusion impedance is almost a straight line and the angle with the real resistance axis is about 70° in the low-frequency area. The ultralow equivalent series resistance (1.27 ohms) and low self-discharge rate (fig. S16) are the main reasons for the excellent electrochemical properties.

The correlations between areal specific capacitance, capacitance retention, and the operating current density of the 3D printing coaxial FASC device are demonstrated in Fig. 4E. The calculated areal specific capacitance of the as-printed device decreases slowly with the increasing current density, leading to excellent rate capability. From Fig. 4F, the fabricated 3D printing coaxial FASC device differs from previous reports in several aspects (*7*, *10*, *14*, *50*–*56*). First, the specific capacitance of the whole device surpasses most of the conventional fiber-shaped supercapacitors. In addition, the electrochemical performances are slightly decreased with the marked increase in the device's length (fig. S17, Supplementary Materials). Then, the as-printed device embraces better cyclic stability than most of the fiber-shaped supercapacitor device, and the capacitance retention of the electrochemical device can achieve 93.1% after 12,000 cycles (fig. S18, Supplementary Materials). Moreover, the device performances, such as areal energy and areal power densities, are revealed in Fig. 4F; the detailed comparison of the areal, volumetric, and gravimetric specific capacitance with corresponding areal, volumetric, and gravimetric energy/power densities is provided in fig. S19 and table S1 (*3*, *5*–*11*, *14*, *16*–*18*, *51*–*56*). Impressively, the printed device delivers the highest E_A of 54.3 μWh cm^{-2} at a P_A of 801.4 μW cm^{-2}, which exceeds most of the reported literature values (*7*, *10*, *14*, *50*–*56*). From the perspective view of flexible and wearable energy storage devices, our 3D printing coaxial FASC device demonstrated both high flexibility and high energy storage capability. Figure S20A demonstrates the CV curves of the device under different bending angles (0° to 180°) at a scan rate of 75 mV s^{-1} (optical images of the device under different bending angles are shown in fig. S21). Obviously, the shapes of the CV curves have no noticeable changes, which indicate that the printed electrochemical device embraces splendid flexibility and excellent mechanical stability. Figure S20B depicts the capacitance retention and specific capacitance of the printed coaxial FASC device under different bending angles at the current density of 1.0 mA cm^{-2}, manifesting the specific capacitance of the as-printed device almost has no decay and the capacitance retention of 97.9% is obtained when the bending angle reaches 180°. In addition, the occlusive areas of the CV curves of the as-printed device have no substantial deviation when the number of bends reaches the 5000th cycle at a scan rate of 75 mV s^{-1} (Fig. 4G). Moreover, the capacitance retention of the printed coaxial FASC device can attain 95.5% of the original specific capacitance after 5000 bending cycles with a bending angle of 90° when the current density is 2.0 mA cm^{-2} (Fig. 4H). The outstanding bending performance is mainly due to the inner and outer PVA gel layers, which take full advantage of the mechanical properties of the wet gel and well maintain the working condition of the device. In addition, the outer layer of the PVA wet gel also prevents the internal electrolyte from evaporating, resulting in better cycling performance of the device. As expected, the 3D printing coaxial FASC device shows low charge transfer resistance and high ionic diffusion behavior (fig. S22, Supplementary Materials), which is due to the compact four-layer structure and shortening of the ion diffusion path within the all-in-one coaxial structure. In addition, the capacitance retention of the device is better than that of the as-fabricated FASC device with twisted and traditional coaxial architectures after numerous bending (bending angle is 90°) (fig. S23A, Supplementary Materials). The SEM images of the different devices before and after bending prove the mechanically robust structure from our FASC device (Fig. S23, B to G, Supplementary Materials). This performance manifests that the 3D printing coaxial FASC device embraces excellent device performance with excellent mechanical property due to the compact structure with a short charge carrier diffusion path. The outstanding mechanical durability is attributed to the intimate interface contact among the positive electrode/electrolyte/negative electrode layers in coaxial FASC devices by the DCMW technology, and the compactly integrated electrode structure can alleviate the mismatch of the Young's modulus from each layer under extreme or repeated bending. To demonstrate the feasibility of powering the electronic devices, a fully charged 3D printing coaxial FASC device with the shape of a dragon can illuminate a 1.5-V red light-emitting diode (LED) (Fig. 4I). Moreover, two 3D printing coaxial FASC devices with gridding shapes in series can illuminate a 3.0-V blue LED, demonstrating the flexibility and wearable capability of 3D printing devices (fig. S24, Supplementary Materials).

Construction of the self-powered and self-monitoring systems and the actual applications in energy storage and conversion

To evaluate this 3D printing coaxial FASC device with high energy density for actual application, we integrate the FASC devices with a solar cell and electric motor to realize the self-powered system, which can convert solar energy into electric energy and, lastly, into mechanical energy (Fig. 5A). To obtain a device with higher energy density to drive the mechanical unit, we constructed the chip-based FASC device by realizing the 3D printing coaxial FASC device in series and the chip-based FASC devices charged by a solar cell that

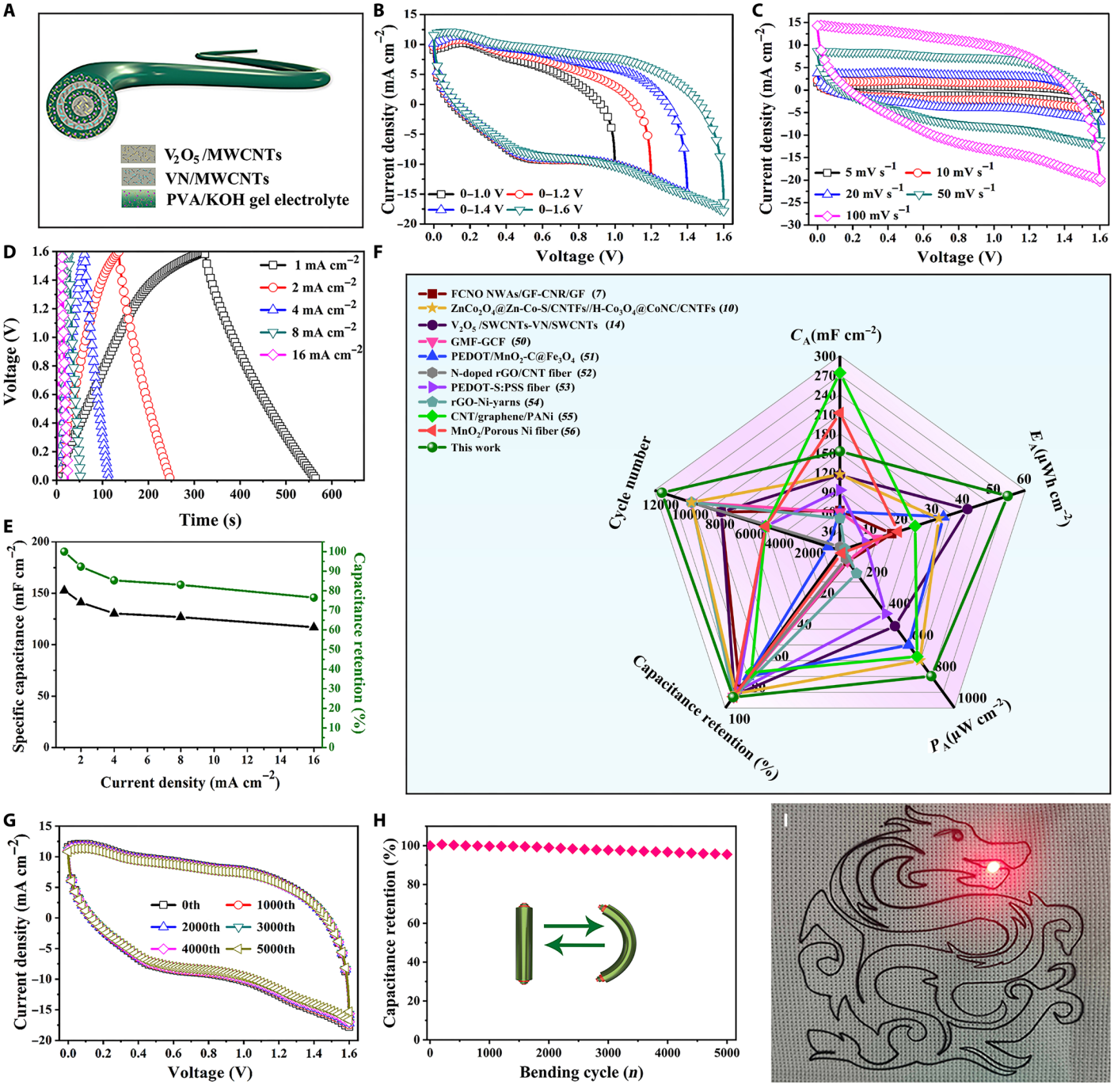

Fig. 4. Electrochemical performance of the 3D printing coaxial FASC device. (**A**) Schematic diagram of the assembled device. (**B**) Cyclic voltammetry (CV) curves of the obtained device operated under different voltage windows. (**C**) CV curves of the device at different scan rates. (**D**) Galvanostatic charge/discharge (GCD) curves of the device at different current densities. (**E**) Rate capability of the device. (**F**) Comparison of electrochemical performance of this 3D printing coaxial FASC device with previous FASC devices (*7*, *10*, *14*, *50*–*56*). Note to the terminology: C_A, areal specific capacitance; E_A, areal energy density; P_A, areal power density. (**G**) CV curves obtained at the different bending cycles at a scan rate of 75 mV s^{-1}. (**H**) Capacitance retention after 5000 cycles. (**I**) Photograph of a red 1.5-V LED illuminated by a fully charged 3D printed coaxial FASC device. Photo credit: (I) Hongyu Lu, Xi'an University of Technology.

can drive the pinwheel for continuous rotation (fig. S25 and movie S2, Supplementary Materials). Meanwhile, the water pumping system can pump more solution when integrating the chip-based FASC device into the solar cell to construct the self-powered system (fig. S26; Fig. 5, B and C; and movies S3 and S4), and the volume of the pumping solution of the self-powered system is more than the device with solar cell only (Fig. 5D). To assess the endurance ability of the self-powered system, the electric car is actuated with and without the chip-based FASC devices. From fig. S27A and movie S5, the electric car with solar cell can merely run a short distance because

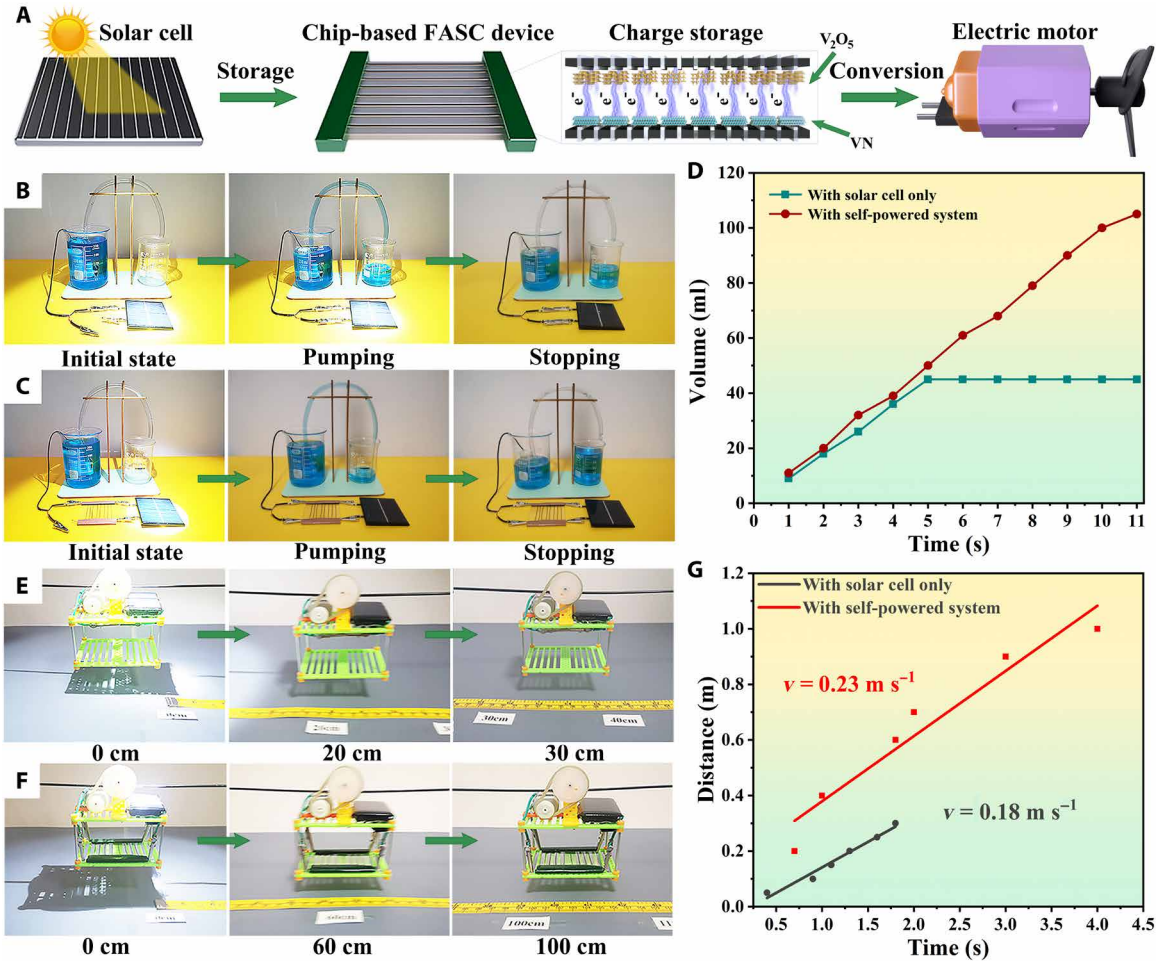

Fig. 5. Applications of the self-powered system. (**A**) Schematic diagram of the self-powered system of energy storage and conversion. The solar energy is converted into electrical energy and then into mechanical energy. (**B**) Photographs of water pumping prototype with solar cell only; less solution is obtained without extra energy. (**C**) Photographs of water pumping prototype with the self-powered configuration including chip-based FASC device and solar cell; more solution is obtained with energy storage. (**D**) Relationship between volume of the pumping solution and time of the solar cell and self-powered system, respectively. (**E**) Photographs of the running of a sightseeing cable car with solar cell only. The sightseeing cable car can run the short distance without extra energy storage. (**F**) Photographs of the running of the sightseeing cable car with the self-powered configuration including chip-based FASC device and solar cell. The sightseeing cable car can run the long distance with energy storage, demonstrating longer durability. (**G**) Relationship between the running distance and time of the sightseeing cable car with self-powered system and solar cell only, respectively. The running speed of the sightseeing cable car with self-powered system is faster than that with solar cell only. Photo credit: (B, C, E, and F) Jingxin Zhao, University of Macau.

of the lack of external energy supply. In contrast, the electric car with the solar cell and the chip-based FASC devices can run a longer distance and even up the ramp, demonstrating enhanced durability for future application in self-powered electric vehicles (figs. S27B and S28A, and movie S6, Supplementary Materials). Furthermore, sightseeing cable cars with a self-powered system embrace faster running speed than that with solar cell only, and the self-powered system can drive the sightseeing cable car with larger resistance to run farther distance, demonstrating the endurance capability of the integrated device (figs. S28B and S29; Fig. 5, E to G; and movies S7 and S8). In addition, the practical functionality of a modern wearable electronic device is important in our daily life. For example, people usually monitor their health status at any time by using the sensors. However, most of the sensors suffer from a limited lifetime, and thus, they have to be charged or replaced frequently. Therefore, our self-energy monitoring system can solve the aforementioned problems (the digital photo is shown in fig. S30). In this integrated device, the as-fabricated 3D printing coaxial FASC device can provide power to the pressure sensor based on bioinspired multiscale structured polydimethylsiloxane (PDMS) and polypyrrole (PPy)/PDMS stamps (Fig. 6A and fig. S31). The as-fabricated pressure sensor can achieve a low pressure of 1.0 Pa, high sensitivity of 70 kPa^{-1} (detection range, <500 Pa), and fast response time (loaded/uploaded time corresponds to 40 and 50 ms, respectively) owing to the existence of the multiscale architecture (fig. S32 and Fig. 6, B to E). Meanwhile, no evident performance degradation is observed after 600 loading/unloading cycles, demonstrating the excellent cycle stability (Fig. 6, F to H). To investigate the sensing capability of the pressure sensor, the pressure sensor is attached to the wrist and fingertip of the tester (an adult female 175 cm in height and 60 kg in weight), and the response signals are detected before and after exercise. Figure 6 (I and J) clearly depicts that both the big and small signals can be monitored, indicating the

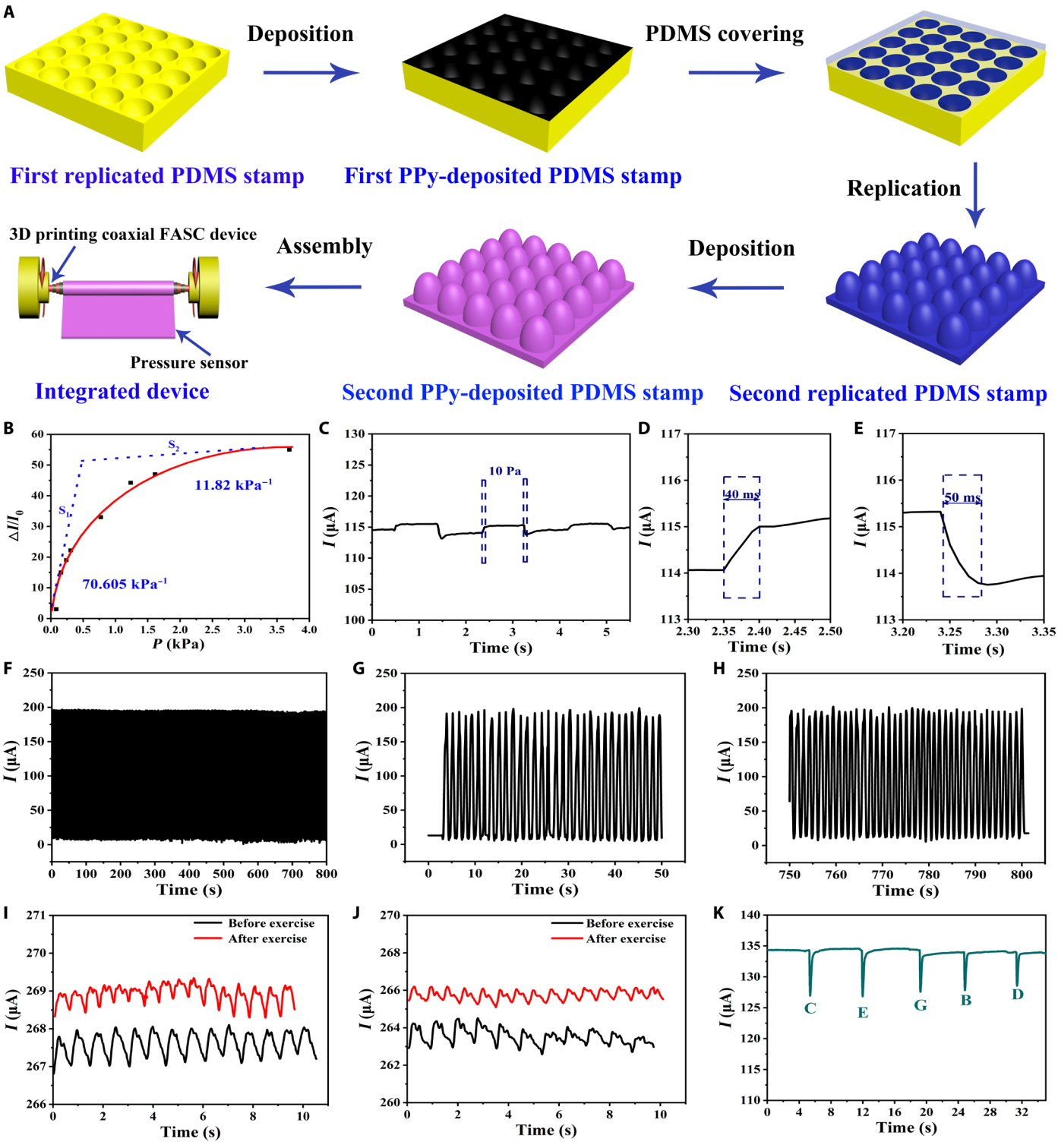

Fig. 6. The sensing performance of the as-fabricated self-energy monitoring system including the 3D printing coaxial FASC device and pressure sensor; the FASC device provide the power to the pressure sensor. (**A**) Schematic diagram of the fabrication process of the self-energy monitoring system. (**B**) Sensitivity of the pressure sensor in the self-energy monitoring system. (**C**) Response signal of the pressure sensor under the 10-Pa pressure in the self-energy monitoring system. The response time of the pressure sensor was tested by placing a weight on the pressure sensor, which is covered by a glass slide to obtain a uniform pressure distribution firstly. (**D** and **E**) Magnified waveforms of the response/relaxation time extracted from (C), respectively. (**F**) Current change of the pressure sensor after repeated loading/uploading the 0.25-kPa pressure in this self-energy monitoring. (**G** and **H**) Magnified waveforms of the first 50 s and the last 50 s obtained from (F), respectively. (**I** and **J**) Response signal of the pressure for the fingertip and wrist pulses before and after exercise. The skin stickers were used to fix the pressure sensor on the fingertip and wrist to obtain a stable pulse signal. (**K**) Response signal of the pressure sensor for five different tones of kalimba piano.

excellent pressure-sensing performance. In addition, the different signals of the purchased kalimba piano can be observed in Fig. 6K, which can be expected to be used in sound recognition. Thus, an all-in-one coaxial solid-state FASC device with high energy density will become a prospective candidate to be used in more new fields such as artificial intelligence, robotics, and sensing.

DISCUSSION

In summary, we developed a 3D printing direct coherent multi-ink writing technology to directly fabricate an all-in-one coaxial solid-state FASC device with an ultrahigh areal energy/power density by designing the internal structure of the multicore-shell needles and regulating the rheological property and the feed rates of the multi-inks. Benefitting from our design of coaxial core-shell configurations, the FASC device with short charge carrier diffusion path has high specific capacitance of 152.7 mF cm^{-2} (C_V of 27.8 F cm^{-3} and C_g of 59.3 F g^{-1}) and splendid areal energy density of 54.3 μWh cm^{-2} (E_V of 9.9 F cm^{-3} and E_g of 21.1 Wh kg^{-1}), as well as an outstanding long cycling life with high capacitance retention of 93.1% after 12,000 cycles. Furthermore, the compact structure of the printed coaxial FASC device embraces splendid flexibility and mechanical stability performance with capacitance retention of 95.5% after 5000 cycles of repetitive bending, which is superior to traditional coaxial or twisted architecture asymmetric supercapacitors. Benefitting from the excellent electrochemical performance, the 3D printing coaxial FASC devices can serve as on-demand energy storage units to drive pinwheels, pumping prototypes, electric cars, and pressure sensors with improved performance. Our developed technology offers a highly versatile and powerful solution to design high-performance on-demand fiber-shaped energy storage devices for advanced wearable electronic applications.

MATERIALS AND METHODS

Preparation of V_2O_5 and VN NWs

V_2O_5 was synthesized via a facile hydrothermal process and subsequent annealing according to the following steps. In a typical fabrication procedure, 0.70 g of the NH_4VO_3 powders was added to 30 ml of distilled water and then stirred for 25 min at room temperature. The solution appears as a clear yellow solution. Then, H_2SO_4 was added into the above solution (pH 1 to 2). The solution was transferred into an 80-ml Teflon-lined autoclave. The autoclave was then maintained at 200°C for 24 hours. The as-prepared product was washed with deionized water and ethanol several times and vacuum dried overnight. Then, the as-prepared V_2O_5 NWs were annealed at 600°C in NH_3 gas for 1 hour to obtain the VN NWs structure.

Preparation of inks

To fabricate the MWCNT-based hybrid inks, the pseudocapacitance substances (V_2O_5 NW or VN NW powder) (200 mg) and MWCNTs (1000 mg) (Chinese Academy of Sciences, Chengdu Organic Chemistry) were added into NMP (10 ml), and the substances were well dispersed in the hybrid suspensions by mechanical agitation and subsequent ultrasonication. Last, the electrode inks were concentrated to 200 mg ml^{-1}. To obtain the PVA/KOH gel electrolyte ink, 10 g of PVA powder and 10 g of KOH were added into 80 g of deionized water, and then gel electrolyte ink was used in the printing process.

3D printing coaxial FASC device by a 3D printing DCMW technology

MWCNT-based inks and gel electrolyte inks were used to construct a 3D printing coaxial FASC device using a robotic deposition device (TH-206H, Tianhao Technic, China). The 3D printing coaxial FASC device was extruded from a coaxial spinneret with no substrate and printed the designed pattern on textiles.

The inks of four injection syringes are V_2O_5 NWs/MWCNTs, PVA/KOH, VN NWs/MWCNTs, and PVA/KOH, respectively, which were connected to the inner (diameter, 250 μm), the second layer (diameter, 270 μm), the third layer (diameter, 390 μm), and the outer (diameter, 400 μm) channels of a coaxial spinneret, respectively. The coaxial spinneret was then fixed onto a 3D printer. Thus, the four inks were synchronously injected to form the coaxial FASC device. The feeding rates of the four ink nozzles were maintained at 10, 15, 20, and 25 ml/hour. The print path of the coaxial spinneret was exactly controlled at a rate of 20 mm/s using a programmed procedure. Last, the 3D printing coaxial FASC device was formed. The various patterns composed of the coaxial FASC devices were directly printed onto the fabric substrate. After printing, the coaxial FASC device or the fabric substrate can be immersed in a PVDF coagulation bath (50 mg ml^{-1}) to remove the solvent followed by washing with ethanol and water and dried for 24 hours at room temperature. In addition, the single fiber electrode (V_2O_5 NW/MWCNT positive electrode or VN NW/MWCNT negative electrode) was obtained by a single spinneret, the feeding rate of the single ink nozzle was maintained at 15 ml/hour, and it can be immersed in a PVDF/NMP coagulation bath (50 mg ml^{-1}); then, NMP solvents were removed by washing with ethanol and water, and dried for 24 hours at room temperature.

FASC device with twisted architecture

The FASC device with twisted architecture was obtained by twisting the 3D printing V_2O_5 NW/MWCNT fiber@gel electrolyte and VN NW/MWCNT fiber@gel electrolyte.

FASC device with the traditional coaxial architecture

The FASC device with the traditional coaxial architecture was obtained by a series of procedures. First, VN NW/MWCNT electrode material was printed in a carbon nanotube (CNT) film. Second, VN NW/MWCNT electrode was wrapped around a 3D printing V_2O_5 NW/MWCNT fiber@gel electrolyte. Last, the second layer gel electrolyte was printed in the as-prepared coaxial FASC device. The length and the mass loading of the FASC with twisted and the traditional coaxial architectures are identical to those of the 3D printing coaxial FASC device.

Fabrication of chip-based FASC device

The chip-based FASC device was assembled by integrating several FASC devices in a series. Then, two conductive copper wires were attached on one side of the chip in parallel.

Assembly of self-powered systems

The self-powered systems were assembled by chip-based FASC device, solar cell, and powered devices such as pinwheel, pumping prototype, electric car, and sightseeing cable car. First, the solar cell was used for harvesting and converted the solar energy into electric energy. Then, the chip-based FASC device was used in storing electric energy, and it can provide power to powered devices.

Fabrication of self-energy monitoring configuration

First, the pressure sensor based on the multiscale structured PPy/PDMS was achieved in accordance with our previously reported procedure (*57*). Then, the as-fabricated pressure sensor was wrapped around the 3D printing coaxial FASC device to form an integrated device. Last, the integrated device was carefully and slightly encapsulated with the scotch tape.

Characterizations

XRD measurements were performed using an x-ray diffractometer using Cu Kα radiation (D8 Advance PANalytical X'Pert Pro). The morphology and microstructures of the samples were observed by a field-emission scanning electron microscope (S-4800) and transmission electron microscope (Tecnai G2 F20 S-TWIN). The Raman spectra of the V_2O_5 NW/MWCNT and VN NW/MWCNT fibers were recorded using a micro-Raman spectroscope (LabRAM HR, with an excitation wavelength of 532 nm). XPS was performed on an ESCALab MKII X-ray photoelectron spectrometer with non-monochromatized Mg-Ka x-ray as the excitation source. The binding energies in the XPS analysis were corrected by referencing C 1s to 284.6 eV. The nitrogen adsorption/desorption measurements were performed on an ASAP 2020 volumetric adsorption analyzer (Micromeritics, USA) at 77 K.

Electrochemical measurements

All electrochemical measurements (CV, GCD, and EIS) were executed to accurately evaluate the electrochemical performance of the single electrodes and the 3D printing coaxial FASC device using an electrochemical working station (CHI760E, Shanghai, China). The single fiber electrodes (fiber positive and negative electrode) were pasted in polyethylene terephthalate (PET) that was stuck on the conductive copper tape for the electrochemical performance measurement. The single-fiber electrodes (fiber positive and negative electrode) were tested in a three-electrode system in 1 M KOH aqueous electrolyte at room temperature; single-fiber electrodes (V_2O_5 NW/MWCNT fiber positive electrode and VN NW/MWCNT fiber negative electrode), a platinum wire electrode, and a saturated calomel electrode (SCE) served as the working electrode, counter electrode, and reference electrode, respectively. The average areal specific capacitance (C_A) values of the single fiber electrodes were calculated from the GCD curves, using the following Eq. 2

$$C_A = \frac{I}{[\mathrm{d}E/\mathrm{d}t]\times A} \approx \frac{I}{[\Delta E/\Delta t]\times A}(\mathrm{mF\ cm^{-2}}) \quad (2)$$

where I is the constant discharge current, Δt is the discharge time interval, A indicates the area of the corresponding single fiber electrodes, and ΔE represents the voltage change after a full discharge.

In a two-electrode system, two copper wires were connected to two electrodes (V_2O_5 NW/MWCNT positive electrode and VN NW/MWCNT negative electrode) to test the 3D printing coaxial FASC device. The average specific capacitance (C_n) values of the 3D printing coaxial FASC device was calculated from GCD curves using the following Eq. 3

$$C_n = \frac{I}{[\mathrm{d}E/\mathrm{d}t]\times n} \approx \frac{I}{[\Delta E/\Delta t]\times n} \quad (3)$$

where I is the constant discharge current, Δt is the discharge time interval, n represents the area (A), mass (m), and volume (V) of the 3D printing coaxial FASC device, and ΔE represents the voltage change after a full discharge.

The energy density and power density of the 3D printing coaxial FASC device were calculated using Eqs. 4 and 5

$$E_n = 0.5\ C_n(\Delta E)^2 \quad (4)$$

$$P_n = \frac{E_n}{t} \quad (5)$$

where E_n indicates the areal energy density (E_A), the gravimetric energy density (E_g), and volumetric energy density (E_V); C_n represents the areal specific capacitance (C_A), gravimetric specific capacitance (C_g), and the volumetric specific capacitance (C_V); ΔE demonstrates the voltage change after a full discharge; P_n manifests the areal power density (P_A), the gravimetric power density (P_g), and the volumetric power density (P_V); and t is the discharge time interval. The cycle-life tests were performed using a LAND system (CTA2001A, China).

The surface area (A) of the 3D printing coaxial FASC device (or single fiber electrodes) was calculated by π multiplied by the diameter (D) of the 3D printing coaxial FASC device (or single fiber electrodes) and the total length (L) of the 3D printing coaxial FASC device. In addition, the volume (V) of the 3D printing coaxial FASC device (or single fiber electrodes) was calculated by π multiplied by the square of the radius (r) of the 3D printing coaxial FASC device (or single fiber electrodes) and the total length of the 3D printing coaxial FASC device or single fiber electrodes. The length of the tested single fiber electrodes and the 3D printing coaxial FASC device are 2.0 and 3.5 cm, respectively. The mass loading of the V_2O_5 NW/MWCNT fiber positive, the VN NW/MWCNT fiber negative electrode, and the 3D printing coaxial FASC device are 4.0, 3.3, and 16.4 mg cm^{-2}, respectively.

For rational design of the FASC devices, the charge match of the negative and positive electrode is important, and the realization of the charge match of negative and positive electrodes is dependent on the designing of the internal structure of the coaxial multicore-shell nozzles. In general, for an asymmetric supercapacitor, the positive charge (Q^+) should be equal to the negative charge (Q^-). The charge (Q) is defined as

$$Q = C \times A \times V \quad (6)$$

where C is the specific capacitance, V is the potential range, and A is the area of the electrode. In the 3D printing coaxial FASC device, the V^+ and V^- are 0.4 and 1.0 V, and C^+ and C^- are 805.6 and 671.2 mF cm^{-2}, respectively. To achieve $Q^+ = Q^-$ at 5 mV s^{-1}, the area balancing between the two electrodes (V_2O_5/MWCNTs and VN/MWCNTs) in the coaxial FASC device should be A (V_2O_5/MWCNT electrode)/A (VN/MWCNT electrode) ≈ 2.04.

The electrical performances of the pressure sensor were also collected by the electrochemical workstation (CHI760E, Shanghai, China). The sensitivity of the pressure sensor was calculated using Eq. 7

$$S = (\Delta I/I_0)/\Delta P \quad (7)$$

where S represents the sensitivity, ΔI demonstrates the current change under a constant pressure load on the pressure sensor, I_0 is

the initial current without pressure load, and ΔP manifests the change of the applied pressure.

SUPPLEMENTARY MATERIALS

Supplementary material for this article is available at http://advances.sciencemag.org/cgi/content/full/7/3/eabd6978/DC1

REFERENCES AND NOTES

1. T. Chen, L. B. Qiu, Z. B. Yang, Z. B. Cai, J. Ren, H. P. Li, H. J. Lin, X. M. Sun, H. S. Peng, An integrated "energy wire" for both photoelectric conversion and energy storage. *Angew. Chem. Int. Ed.* **51**, 11977–11980 (2012).
2. J. Ren, L. Li, C. Chen, X. L. Chen, Z. B. Cai, L. B. Qiu, Y. G. Wang, X. R. Zhu, H. S. Peng, Twisting carbon nanotube fibers for both wire-shaped micro-supercapacitor and micro-battery. *Adv. Mater.* **25**, 1155–1159 (2013).
3. P. P. Shi, L. Li, L. Hua, Q. Q. Qian, P. F. Wang, J. Y. Zhou, G. Z. Sun, W. Huang, Design of amorphous manganese oxide@multiwalled carbon nanotube fiber for robust solid-state supercapacitor. *ACS Nano* **11**, 444–452 (2017).
4. Z. Wen, M.-H. Yeh, H. Y. Guo, J. Wang, Y. L. Zi, W. D. Xu, J. N. Deng, L. Zhu, X. Wang, C. G. Hu, L. P. Zhu, X. H. Sun, Z. L. Wang, Self-powered textile for wearable electronics by hybridizing fiber-shaped nanogenerators, solar cells, and supercapacitors. *Sci. Adv.* **2**, e1600097 (2016).
5. K. Lu, J. T. Zhang, Y. Q. Wang, J. Z. Ma, B. Song, H. Y. Ma, Interfacial deposition of three-dimensional nickel hydroxide nanosheet-graphene aerogel on Ni wire for flexible fiber asymmetric supercapacitors. *ACS Sustainable Chem. Eng.* **5**, 821–827 (2017).
6. Q. Liu, J. W. Zhou, C. H. Song, X. L. Li, Z. P. Wang, J. Yang, J. L. Cheng, H. Li, B. Wang, 2.2 V high performance symmetrical fiber-shaped aqueous supercapacitors enabled by "water-in-salt" gel electrolyte and N-Doped graphene fiber. *Energy Storage Mater.* **24**, 495–503 (2020).
7. J. X. Zhao, C. W. Li, Q. C. Zhang, J. Zhang, X. N. Wang, J. Sun, J. J. Wang, J. X. Xie, Z. Y. Lin, Z. Li, W. B. Lu, C. H. Lu, Y. G. Yao, Hierarchical ferric-cobalt-nickel ternary oxide nanowire arrays supported on graphene fibers as high-performance electrodes for flexible asymmetric supercapacitors. *Nano Res.* **11**, 1775–1786 (2018).
8. J. L. Yu, W. B. Lu, J. P. Smith, K. S. Boosh, L. H. Meng, Y. D. Huang, Q. W. Li, J.-H. Byun, Y. S. Oh, Y. S. Yan, T.-W. Chou, A high performance stretchable asymmetric fiber-shaped supercapacitors with a core-sheath helical structure. *Adv. Funct. Mater.* **7**, 1600976 (2017).
9. Y. F. Zhang, X. Y. Zhang, K. Yang, X. L. Fan, Y. X. Tong, Z. S. Zhang, X. H. Lu, K. C. Mai, Q. Q. Ni, M. Q. Zhang, X. D. Chen, Ultrahigh energy fiber-shaped supercapacitors based on porous hollow conductive polymer composite fiber electrodes. *J. Mater. Chem. A* **6**, 12250–12258 (2018).
10. J. X. Zhao, H. Y. Li, C. W. Li, Q. C. Zhang, J. Sun, X. N. Wang, J. B. Guo, L. Y. Xie, B. He, Z. Y. Zhou, C. H. Lu, W. B. Lu, G. Zhu, Y. G. Yao, MOF for template-directed growth of well-oriented nanowire hybrid arrays on carbon nanotube fibers for wearable electronics integrated with triboelectric nanogenerators. *Nano Energy* **45**, 420–431 (2018).
11. M. M. Liu, Z. F. Cong, X. Pu, W. B. Guo, T. Liu, M. Li, Y. Zhang, W. G. Hu, Z. L. Wang, High-energy asymmetric supercapacitor yarns for self-charging power textiles. *Adv. Funct. Mater.* **29**, 1806298 (2019).
12. Q. C. Zhang, W. W. Xu, J. Sun, Z. H. Pan, J. X. Zhao, X. N. Wang, J. Zhang, P. Man, J. B. Guo, Z. Y. Zhou, B. He, Z. X. Zhang, Q. W. Li, Y. G. Zhang, L. Xu, Y. G. Yao, Constructing ultrahigh-capacity zinc-nickel-cobalt Oxide@Ni(OH)$_2$ core–shell nanowire arrays for high-performance coaxial fiber-shaped asymmetric supercapacitors. *Nano Lett.* **17**, 7552–7560 (2017).
13. Z. H. Pan, J. Zhong, Q. C. Zhang, J. Yang, Y. C. Qiu, X. Y. Ding, K. Q. Nie, H. Yuan, K. Feng, X. S. Wang, G. G. Xu, W. F. Li, Y. G. Yao, Q. W. Li, M. N. Liu, Y. G. Zhang, Ultrafast all-solid-state coaxial asymmetric fiber supercapacitors with a high volumetric energy density. *Adv. Energy Mater.* **8**, 1702946 (2018).
14. J. X. Zhao, Y. Zhang, Y. N. Huang, J. X. Xie, X. X. Zhao, C. W. Li, J. Y. Qu, Q. C. Zhang, J. Sun, B. He, Q. L. Li, C. H. Lu, X. H. Xu, W. B. Lu, L. Q. Li, Y. G. Yao, 3D printing fiber electrodes for an all-fiber integrated electronic device via hybridization of an asymmetric supercapacitor and a temperature sensor. *Adv. Sci.* **5**, 1801114 (2018).
15. J. X. Zhao, Y. Zhang, X. X. Zhao, R. T. Wang, J. X. Xie, C. F. Yang, J. J. Wang, Q. C. Zhang, L. L. Li, C. H. Lu, Y. G. Yao, Direct ink writing of adjustable electrochemical energy storage device with high gravimetric energy densities. *Adv. Funct. Mater.* **29**, 1900809 (2019).
16. T. Chen, L. M. Dai, Flexible and wearable wire-shaped microsupercapacitors based on highly aligned titania and carbon nanotubes. *Energy Storage Mater.* **2**, 21–26 (2016).
17. Y. Q. Guo, X. F. Hong, Y. Wang, Q. Li, J. S. Meng, R. T. Dai, X. Liu, L. He, L. Q. Mai, Multicomponent hierarchical Cu-doped NiCo-LDH/CuO double arrays for ultralong-life hybrid fiber supercapacitor. *Adv. Funct. Mater.* **29**, 1809004 (2019).
18. N. Yu, H. Yin, W. Zhang, Y. Liu, Z. Y. Tang, M.-Q. Zhu, High-performance fiber-shaped all-solid-state asymmetric supercapacitors based on ultrathin MnO_2 nanosheet/carbon fiber cathodes for wearable electronics. *Adv. Energy Mater.* **6**, 1501458 (2019).
19. Y. B. Wang, C. J. Chen, H. Xie, T. T. Gao, Y. G. Yao, G. Pastel, X. G. Han, Y. J. Li, J. P. Zhao, K. Fu, L. B. Hu, 3D-printed all-fiber li-ion battery toward wearable energy storage. *Adv. Funct. Mater.* **27**, 1703140 (2017).
20. J. Mueller, J. R. Raney, K. Shea, J. A. Lewis, Architected lattices with high stiffness and toughness via multicore-shell 3D printing. *Adv. Mater.* **30**, 1705001 (2018).
21. A. Lee, A. R. Hudson, D. J. Shiwarski, J. W. Tashman, T. J. Hinton, S. Yerneni, J. M. Bliley, P. G. Campbell, A. W. Feinberg, 3D bioprinting of collagen to rebuild components of the human heart. *Science* **365**, 482–487 (2019).
22. B. Derby, Printing and prototyping of tissues and scaffolds. *Science* **338**, 921–926 (2012).
23. D. A. Walker, J. L. Hedrick, C. A. Mirkin, Rapid, large-volume, thermally controlled 3D printing using a mobile liquid interface. *Science* **366**, 360–364 (2019).
24. S. Gantenbein, K. Masania, W. Woigk, J. P. W. Sesseg, T. A. Tervoort, A. R. Studart, Three-dimensional printing of hierarchical liquid-crystal-polymer structures. *Nature* **561**, 226–230 (2018).
25. M. A. Skylar-Scott, J. Mueller, C. W. Visser, J. A. Lewis, Voxelated soft matter via multimaterial multinozzle 3D printing. *Nature* **575**, 330–335 (2019).
26. H. Yuk, B. Lu, S. Lin, K. Qu, J. Xu, J. Luo, X. Zhao, 3D printing of conducting polymers. *Nat. Commun.* **11**, 1604 (2020).
27. J. U. Lind, T. A. Busbee, A. D. Valentine, F. S. Pasqualini, H. Y. Yuan, M. Yadid, S.-J. Park, A. Kotikian, A. P. Nesmith, P. H. Campbell, J. J. Vlassak, J. A. Lewis, K. K. Parker, Instrumented cardiac microphysiological devices via multimaterial three-dimensional printing. *Nat. Mater.* **16**, 303–308 (2017).
28. R. L. Truby, M. Wehner, A. K. Grosskopf, D. M. Vogt, S. G. M. Uzel, R. J. Wood, J. A. Lewis, Soft somatosensitive actuators via embedded 3D printing. *Adv. Mater.* **30**, 1706383 (2018).
29. K. Fu, Y. G. Yao, J. Q. Dai, L. B. Lu, Progress in 3D printing of carbon materials for energy-related applications. *Adv. Mater.* **29**, 1603486 (2017).
30. J. N. Gu, Q. Zhu, Y. Z. Shi, H. Chen, D. Zhang, Z. G. Du, S. B. Yang, Single zinc atoms immobilized on MXene ($Ti_3C_2Cl_x$) layers toward dendrite-free lithium metal anodes. *ACS Nano* **14**, 891–898 (2020).
31. K. Sun, T.-S. Wei, B. Y. Ahn, J. Y. Seo, S. J. Dillon, J. A. Lewis, 3D Printing of interdigitated Li-ion microbattery architectures. *Adv. Mater.* **25**, 4539–4543 (2013).
32. B. Yao, S. Chandrasekaran, J. Zhang, W. Xiao, F. Qian, C. Zhu, E. B. Duoss, C. M. Spadaccini, M. A. Worsley, Y. Li, Efficient 3D printed pseudocapacitive electrodes with ultrahigh MnO_2 loading. *Joule* **3**, 459–470 (2019).
33. Y. Zhang, T. X. Ji, S. H. Hou, L. F. Zhang, Y. H. Shi, J. X. Zhao, X. H. Xu, All-printed solid-state substrate-versatile and high-performance micro-supercapacitors for in situ fabricated transferable and wearable energy storage via multi-material 3D printing. *J. Power Sources* **403**, 109–117 (2018).
34. S. C. Ligon, R. Liska, J. Stampfl, M. Gurr, R. Mulhaupt, Polymers for 3D printing and customized additive manufacturing. *Chem. Rev.* **117**, 10212–10290 (2017).
35. Y. Jiang, Z. Xu, T. Huang, Y. Liu, F. Guo, J. Xi, W. Guo, C. Gao, Direct 3D printing of ultralight graphene oxide aerogel microlattices. *Adv. Funct. Mater.* **28**, 1707024 (2018).
36. B. Yan, X. F. Li, Z. M. Bai, Y. Zhao, L. Dong, X. S. Song, D. J. Li, C. Langford, X. L. Sun, Crumpled reduced graphene oxide conformally encapsulated hollow V_2O_5 nano/microsphere achieving brilliant lithium storage performance. *Nano Energy* **24**, 32–44 (2016).
37. F. Y. Cheng, T. R. Zhang, Y. Zhang, J. Du, X. P. Han, J. Chen, Enhancing electrocatalytic oxygen reduction on MnO_2 with vacancies. *Angew. Chem. Int. Ed.* **52**, 2474–2477 (2013).
38. J. O. Hardin, T. J. Ober, A. D. Valentine, J. A. Lewis, Microfluidic printheads for multimaterial 3D printing of viscoelastic inks. *Adv. Mater.* **27**, 3279–3284 (2015).
39. J. X. Zhao, C. W. Li, Q. C. Zhang, J. Zhang, X. N. Wang, Z. Y. Lin, J. J. Wang, W. B. Lu, C. H. Lu, C.-P. Wong, Y. G. Yao, An all-solid-state, lightweight, and flexible asymmetric supercapacitor based on cabbage-like $ZnCo_2O_4$ and porous VN nanowires electrode materials. *J. Mater. Chem. A* **5**, 6928–6936 (2017).
40. R. T. Wang, J. W. Lang, P. Zhang, Z. Y. Lin, X. B. Yan, Fast and large lithium storage in 3D porous VN nanowires-graphene composite as a superior anode toward high-performance hybrid supercapacitors. *Adv. Funct. Mater.* **25**, 2270–2278 (2015).
41. R. T. Wang, J. W. Lang, P. Zhang, Z. Y. Lin, X. B. Yan, Coupling effect between ultra-small Mn_3O_4 nanoparticles and porous carbon microrods for hybrid supercapacitors. *Energy Storage Mater.* **6**, 53–60 (2017).
42. T. Cheng, Y.-W. Wu, Y.-L. Chen, Y.-Z. Zhang, W.-Y. Lai, W. Huang, Inkjet-printed high-performance flexible micro-supercapacitors with porous nanofiber-like electrode structures. *Small* **15**, 1901830 (2019).
43. H. Sun, X. You, J. Deng, X. L. Chen, Z. B. Yang, J. Ren, H. S. Peng, Novel graphene/carbon nanotube composite fibers for efficient wire-shaped miniature energy devices. *Adv. Mater.* **26**, 2868–2873 (2014).

44. Y.-Z. Zhang, T. Cheng, Y. Wang, W.-Y. Lai, H. Pang, W. Huang, A simple approach to boost capacitance: flexible supercapacitors based on manganese Oxides@MOFs via chemically induced in situ self-transformation. *Adv. Mater.* **28**, 5242–5248 (2016).
45. M. H. Yu, X. L. Feng, Thin-film electrode-based supercapacitors. *Joule* **3**, 338–360 (2019).
46. Y.-Z. Zhang, Y. Wang, T. Cheng, L.-Q. Yao, X. C. Li, W.-Y. Lai, W. Huang, Printed supercapacitors: Materials, printing and applications. *Chem. Soc. Rev.* **48**, 3229–3264 (2019).
47. W. B. Yan, T. Ayvazian, J. Y. Kim, Y. Liu, K. C. Donavan, W. D. Xing, Y. G. Yang, J. C. Hemminger, R. M. Penner, Mesoporous manganese oxide nanowires for high-capacity, high-rate, hybrid electrical energy storage, hybrid electrical energy storage. *ACS Nano* **5**, 8275–8287 (2011).
48. L. Q. Yao, T. Cheng, X. Q. Shen, Y. Z. Zhang, W. Y. Lai, W. Huang, Paper-based all-solid-state flexible asymmetric micro-supercapacitors fabricated by a simple pencil drawing methodology. *Chin. Chem. Lett.* **29**, 587–591 (2018).
49. Y.-Z. Zhang, Y. Wang, T. Cheng, W.-Y. Lai, H. Pang, W. Huang, Flexible supercapacitors based on paper substrates: A new paradigm for low-cost energy storage. *Chem. Soc. Rev.* **44**, 5181–5199 (2015).
50. B. Zheng, T. Huang, L. Kou, X. Zhao, K. Gopalsamy, C. Gao, Graphene fiber-based asymmetric micro-supercapacitors. *J. Mater. Chem. A* **2**, 9736–9743 (2014).
51. J. F. Sun, Y. Huang, C. X. Fu, Y. Huang, M. S. Zhu, X. M. Tao, C. Y. Zhi, H. Hu, A high performance fiber-shaped PEDOT@MnO_2//C@Fe_3O_4 asymmetric supercapacitor for wearable electronics. *J. Mater. Chem. A* **4**, 14877–14883 (2016).
52. D. Yu, S. Zhai, W. Jiang, K. Goh, L. Wei, X. Chen, R. Jiang, Y. Chen, Transforming pristine carbon fiber tows into high performance solid-state fiber supercapacitors. *Adv. Mater.* **27**, 4895–4901 (2015).
53. Z. P. Wang, J. L. Cheng, Q. Guan, H. Huang, Y. C. Li, J. W. Zhou, W. Ni, B. Wang, S. S. He, H. S. Peng, All-in-one fiber for stretchable fiber-shaped tandem supercapacitors. *Nano Energy* **45**, 210–219 (2018).
54. X. Pu, L. X. Li, M. M. Liu, C. Y. Jiang, C. H. Du, Z. F. Zhao, W. G. Hu, Z. L. Wang, Wearable self-charging power textile based on flexible yarn supercapacitors and fabric nanogenerators. *Adv. Mater.* **28**, 98–105 (2016).
55. Z. Lu, J. Foroughi, C. Y. Wang, H. R. Long, G. G. Wallace, Superelastic hybrid CNT/graphene fibers for wearable energy storage. *Adv. Energy Mater.* **8**, 1702047 (2018).
56. P. Li, J. Li, Z. Zhao, Z. S. Fang, M. J. Yang, Z. K. Yuan, Y. Zhang, Q. Zhang, W. Hong, X. D. Chen, D. S. Yu, A general electrode design strategy for flexible fiber micro-pseudocapacitors combining ultrahigh energy and power delivery. *Adv. Sci.* **4**, 1700003 (2017).
57. S. X. Yu, L. L. Li, J. J. Wang, E. P. Liu, J. X. Zhao, F. Xu, Y. P. Cao, C. H. Lu, Light-boosting highly sensitive pressure sensors based on bioinspired multiscale surface structures. *Adv. Funct. Mater.* **30**, 1907091 (2020).

Acknowledgments

Funding: This work was funded by the Science and Technology Development Fund, Macau SAR (file nos. 0057/2019/A1 and 0092/2019/A2), the startup grant from Fuzhou University, and the National Nature Science Foundation of China (grant no. 21875040). **Author contributions:** Y.T., X.C., and J.P. proposed and supervised this project. J.Z., H.L., Yan Zhang, and S.Y. designed the experiments and wrote the manuscript. O.I.M. and X.Z. contributed to the writing of the manuscript. L.W., H.W., X.L., Yanyan Zhang, S.C., and H.P. participated in analyzing and G.X. and C.L. in discussing the experimental results. **Competing interests:** Y.T., J.Z., and H.L. are inventors on a pending patent filed by the State Intellectual Property Office of China (no. 2020110348882, filed 27 September 2020). The other authors declare that they have no competing interests. **Data and materials availability:** All data needed to evaluate the conclusions in the paper are present in the paper and/or the Supplementary Materials. Additional data related to this paper may be requested from the authors.

Submitted 7 July 2020
Accepted 25 November 2020
Published 15 January 2021
10.1126/sciadv.abd6978

Citation: J. Zhao, H. Lu, Y. Zhang, S. Yu, O. I. Malyi, X. Zhao, L. Wang, H. Wang, J. Peng, X. Li, Y. Zhang, S. Chen, H. Pan, G. Xing, C. Lu, Y. Tang, X. Chen, Direct coherent multi-ink printing of fabric supercapacitors. *Sci. Adv.* **7**, eabd6978 (2021).